

## Ultrasound-based relative elastic modulus imaging for visualizing thermal ablation zones in a porcine model

This article has been downloaded from IOPscience. Please scroll down to see the full text article.

2010 Phys. Med. Biol. 55 2281

(<http://iopscience.iop.org/0031-9155/55/8/011>)

View [the table of contents for this issue](#), or go to the [journal homepage](#) for more

Download details:

IP Address: 128.104.2.244

The article was downloaded on 15/07/2010 at 21:04

Please note that [terms and conditions apply](#).

## Ultrasound-based relative elastic modulus imaging for visualizing thermal ablation zones in a porcine model

Jingfeng Jiang<sup>1,6</sup>, Chris Brace<sup>1,2,3</sup>, Anita Andreano<sup>2,5</sup>,  
Ryan J DeWall<sup>1,3</sup>, Nick Rubert<sup>1</sup>, Ted G Fisher<sup>1</sup>, Tomy Varghese<sup>1,3,4</sup>,  
Fred Lee Jr<sup>2</sup> and Timothy J Hall<sup>1</sup>

<sup>1</sup> Department of Medical Physics, University of Wisconsin-Madison, WIMR-1005,  
1111 Highland Ave., Madison, WI 53705, USA

<sup>2</sup> Department of Radiology, University of Wisconsin-Madison, Madison, WI 53792, USA

<sup>3</sup> Department of Biomedical Engineering, University of Wisconsin-Madison, Madison,  
WI 53706, USA

<sup>4</sup> Department of Electrical and Computer Engineering, University of Wisconsin-Madison,  
Madison, WI 53706, USA

<sup>5</sup> Department of Radiology, University of Milan-Bicocca, Milan, Italy

E-mail: [jjiang2@wisc.edu](mailto:jjiang2@wisc.edu)

Received 9 October 2009, in final form 24 February 2010

Published 30 March 2010


Online at [stacks.iop.org/PMB/55/2281](http://stacks.iop.org/PMB/55/2281)

### Abstract

The feasibility of using ultrasound-based elastic modulus imaging to visualize thermal ablation zones in an *in vivo* porcine model is reported. Elastic modulus images of soft tissues are estimated as an inverse optimization problem. Ultrasonically measured displacement data are utilized as inputs to determine an elastic modulus distribution that provides the best match to this displacement field. A total of 14 *in vivo* thermal ablation zones were investigated in this study. To determine the accuracy of delineation of each thermal ablation zone using elastic modulus imaging, the dimensions (lengths of long and short axes) and the area of each thermal ablation zone obtained from an elastic modulus image were compared to the corresponding gross pathology photograph of the same ablation zone. Comparison of elastic modulus imaging measurements and gross pathology measurements showed high correlation with respect to the area of thermal ablation zones (Pearson coefficient = 0.950 and  $p < 0.0001$ ). The radiological–pathological correlation was slightly lower (correlation = 0.853,  $p < 0.0001$ ) for strain imaging among these 14 *in vivo* ablation zones. We also found that, on average, elastic modulus imaging can more accurately depict thermal ablation zones, when compared to strain imaging (14.7% versus 22.3% absolute percent error in area measurements, respectively). Furthermore, elastic modulus imaging also provides higher (more than a factor of 2) contrast-to-noise ratios for evaluating these thermal ablation zones than those on corresponding strain images, thereby reducing

<sup>6</sup> Author to whom any correspondence should be addressed.

inter-observer variability. Our preliminary results suggest that elastic modulus imaging might potentially enhance the ability to visualize thermal ablation zones, thereby improving assessment of ablative therapies.

 Online supplementary data available from [stacks.iop.org/PMB/55/2281/mmedia](https://stacks.iop.org/PMB/55/2281/mmedia)

(Some figures in this article are in colour only in the electronic version)

## 1. Introduction

Image-guided radiofrequency (RF) and microwave (MW) ablation are increasingly used to treat primary and some metastatic tumors in the liver (Sato *et al* 1996, Lencioni *et al* 2005, Lu *et al* 2005, Liang *et al* 2005). In recent reports, excellent outcomes of treating renal tumors using RF and MW ablation techniques were also achieved by several groups (Gervais *et al* 2000, 2005, Zagoria *et al* 2007, Laeseke *et al* 2007). The clinical potential of these techniques for treatment of neoplasms at other sites, including breast (Jeffrey *et al* 1999), bone (Rosenthal *et al* 1998, Callstrom *et al* 2006) and lung (Nguyen *et al* 2005, Wolf *et al* 2008, White and D'Amico 2008), has also been reported. While thermal ablation can be an effective cancer treatment tool, the lack of a reliable imaging modality to monitor progression of ablation treatment is still a significant problem (Gazelle *et al* 2000, Solbiati *et al* 1997, Goldberg *et al* 2000, Montgomery *et al* 2004). To eradicate the entire tumor mass, thermal ablation must ensure delivery of a lethal thermal dose to the whole tumor and an ablative margin, while minimizing heat damage to vulnerable areas (e.g. bowel, stomach, gall bladder, bile ducts and the renal cortex). Unfortunately, because of a lack of adequate imaging-based treatment monitoring options, undertreated portions of the tumor often go undetected until follow-up. Accordingly, a rapid feedback imaging technique would be useful for the real-time or near real-time evaluation of the ablation zone to help reduce the number of local recurrences and subsequent re-treatment sessions after thermal tumor ablation.

In many centers, the insertion of the RF/MW applicator is usually done under ultrasound guidance since it offers a fast and effective real-time method of guidance. Unfortunately, attempts to monitor ablation with conventional B-mode ultrasound have been largely unsuccessful. Hyperechoic areas caused by micro-bubbles and gas formed during tissue heating have been used as a surrogate for the ablation zone but do not correlate well with the actual ablation zone (Bush *et al* 1993). In addition, these hyperechoic areas gradually disappear within 30 min after ablation, making post-treatment evaluation difficult. Contrast-enhanced ultrasound (CEUS) has been shown to be of benefit (Solbiati *et al* 2004) but is not approved for use in all countries. CEUS is also plagued by a relatively short cycle time in the livers and kidneys. In addition, to monitor an ablation procedure, micro-bubble contrast agents must thereafter be continuously injected throughout the treatment.

X-ray computed tomography (CT) can predict the coagulation zone with a precision of 2–3 mm (Goldberg *et al* 2000). However, the use of CT or contrast-enhanced CT (Dupuy and Goldberg 2001) is limited by the amount of contrast agent that can be injected (due to possible renal failure) and concerns regarding the radiation dose to both the patient and the physician. Magnetic resonance imaging (MRI) can be utilized for imaging the ablation zone in several ways (Goldberg *et al* 1998, Weidensteiner *et al* 2003, Stern *et al* 2008, Pilatou *et al* 2009, Hyodoh *et al* 1998). However, there is limited availability of FDA-approved MRI-compatible applicators and a shortage of interventional MRI scanners (Carter *et al* 1998, Wacker *et al* 2004).

During RF ablation, protein denaturation during heating results in an increase in the elastic modulus of tissue (Kiss *et al* 2004). Therefore, thermal ablation zones appear to be stiffer than surrounding untreated tissue and may be differentiated by new elasticity imaging methods that directly estimate mechanical properties of soft tissue (Gao *et al* 1996, Greenleaf *et al* 2003, Ophir *et al* 1999, Hall 2003). Several methods, including strain imaging (Varghese *et al* 2002, Kallel *et al* 1999), sonoelastography (Zhang *et al* 2008) and acoustic radiation force imaging (Fahey *et al* 2006), have demonstrated good correspondence between elasticity imaging findings and gross pathology features.

Our group, among others, has been developing quasi-static elasticity imaging methods that employ unmodified clinical equipment and examination techniques similar to standard clinical ultrasound examinations. With these methods, an ultrasound transducer is used to acquire phase-sensitive ultrasound echo data (either radiofrequency (RF) or quadrature data). Ultrasound echo signals are tracked as the anatomy is deformed to obtain local tissue displacement information. The displacement field is then used to calculate the component of strain along the direction of the acoustic beam (hereafter referred as to strain) to form a 2D/3D strain image. This strain image is interpreted as an image of the reciprocal of the shear or Young's modulus for the tissue (Ophir *et al* 1991). Unlike strain, Young's or shear modulus is an intrinsic material property of the tissue being studied, thereby providing unambiguous information regarding tissue elasticity (Barbone and Bamber 2002). Considerable research efforts have been directed to use the same displacement field to solve an inverse elasticity problem to explicitly determine the spatial distribution of the elastic modulus of interest. While a few techniques (Kallel and Bertrand 1996, Zhu *et al* 2003, Doyley *et al* 2000, Oberai *et al* 2004) have been proposed, only few applications to date (Oberai *et al* 2009) have been applied to *in vivo* soft tissue. In this study, we will apply our relative elastic modulus imaging (EMI) technique specifically designed for using ablation applicator-induced deformation (Jiang *et al* 2009) in an *in vivo* porcine liver model.

Our objective is to evaluate the radiological–pathological correlation and accuracy of this technique in pre-clinical animal studies. In this paper, we compare the dimension and area measurements of *in vivo* thermal ablation zones obtained using strain imaging and relative EMI against the dimension and area measurements using corresponding gross-pathology photographs of the same thermal ablation zones. Furthermore, both a contrast-noise ratio metric (Song *et al* 2004) and inter-observer variability among three human observers of elastic modulus and strain images are assessed to demonstrate that the EMI could become a potentially enhanced modality for visualizing thermal ablation zones.

## 2. Materials and methods

A brief description of the proposed EMI method including data acquisition and analysis is given in this section. Figure 1 shows a flowchart describing, in general, the proposed EMI method used for data acquisition and processing.

### 2.1. Animal preparation and experiments

Following an institutionally approved animal protocol, a total of 15 ablation zones were created *in vivo* in five porcine animals with normal liver (radiofrequency  $n = 14$  and microwave  $n = 1$ ). During open-abdomen ablation experiments, general anesthesia was first induced with an intramuscular injection of teletamine and zolazepam (Telazol; Fort Dodge Laboratories, Fort Dodge, IA) and xylazine (Rompun; Bayer Corporation, Shawnee Mission, KS) and was maintained with inhaled isoflurane 1–3%. Subsequently, laparotomy

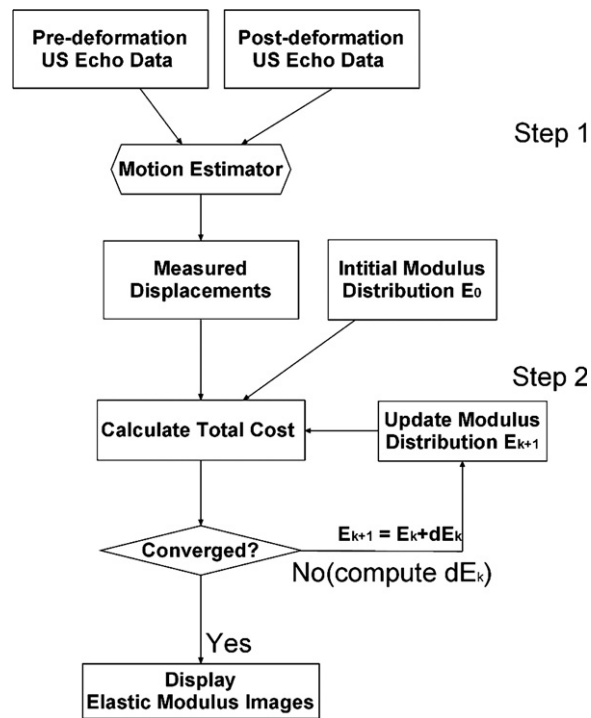
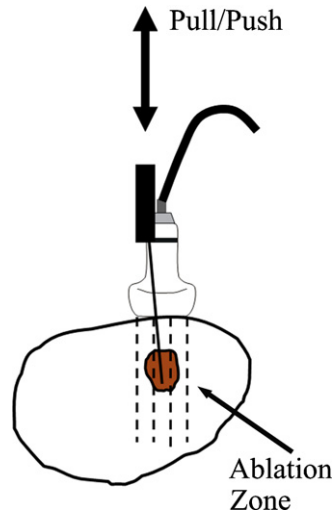


Figure 1. A flowchart describing the EMI procedure.

was performed for each animal to expose the liver for open abdominal ablation. Fourteen radiofrequency ablation procedures were performed using a 17-gauge cooled needle electrode (Valleylab Inc., CO, USA) with a 30 mm electrically active tip, while the only microwave ablation experiment was performed using a 17-gauge triaxial antenna prototype (Brace *et al* 2007). Ablation experiments were performed for 4–12 min to create various sized thermal ablation zones (1–3 cm diameter).

Immediately following each ablation procedure, the hand-held ultrasound transducer was positioned adjacent to the ablation applicator, and a radiologist (AA) first scanned the entire thermal ablation zone. After identification of an appropriate imaging plane by the radiologist for each ablation zone, ultrasound echo data were collected under the guidance of a real-time strain imaging system (eSie Touch, Siemens Antares, Siemens Healthcare Inc., Ultrasound Division). During ultrasound data acquisition, an RF or MW applicator was used to perturb liver tissues to create the deformations needed for strain imaging and EMI as shown in figure 2 (Varghese *et al* 2002). Of note, small (<0.5 mm from (ultrasound) frame-to-frame) deformation of the tissue was achieved by pulling or pushing the ablation electrode enabling a deformation force to be transmitted to the tissue being imaged through the adherence of ablated soft tissue to the metal electrode (Mikami *et al* 2004). All ultrasound data were acquired using a linear array ultrasound transducer (VFX 9–4; Siemens Healthcare (USA) Inc.) pulsed at 6 MHz in conjunction with the Axius Direct™ Ultrasound Research Interface (URI) package (Brunke *et al* 2007). The lateral beam spacing and axial sample size for the ultrasound data acquired were approximately 0.15 mm and 0.02 mm, respectively.

After each animal was euthanized, the entire liver was removed and was serially sectioned at approximately 3 mm intervals to expose the ultrasound imaging plane for gross pathology



**Figure 2.** A schematic diagram illustrating the experimental setup for ultrasound data acquisition using RF electrode deformation. The arrow points to the thermal ablation zone (the shadowed area). Ultrasound echo data are acquired from the area covered by the dashed lines using a linear array ultrasound transducer.

analysis. Section planes of each ablation zone were nearly parallel to the corresponding insertion track of the ablation applicator and were determined under the guidance of surface markers representing the corresponding imaging plane.

## 2.2. Formation of strain and elastic modulus images

As illustrated in figure 1, in the first step, a previously published speckle tracking method (Jiang and Hall 2009) was used to obtain the ultrasonically measured displacement field. These displacement measurements were then used as inputs for the inverse reconstruction of the modulus distribution in the second step. This speckle tracking algorithm is a constrained block matching algorithm (BMA) that tracks ultrasonic speckle patterns by searching for a kernel of echo data from the pre-compression echo data in a 2D search region of the post-compression echo field to minimize the following cost function:

$$\text{COST} = \sum_{\Omega} (\alpha E_C + \Phi(E_S)), \quad (1)$$

where the first item  $E_C$  is a penalty term for speckle de-correlation, the second term  $\Phi(E_S)$  is a penalty term due to the loss of motion continuity from a cluster of displacement vectors, and  $\alpha$  is a positive regularization parameter. We set  $\alpha$  to 1 for all data investigated in this paper.

Using axial (parallel to the acoustic beam direction) displacements obtained from the above-described speckle tracking algorithm, a 2D finite element-based iterative modulus reconstruction algorithm developed in our previous work (Jiang *et al* 2009) was used to obtain modulus distributions in and around all 14 thermal ablation zones. The basic idea of EMI is to iteratively adjust local modulus values to enforce a biomechanical model to produce displacements close to those obtained from ultrasonic speckle tracking. We formulate the EMI as a constrained minimization problem and assume that the tissue being imaged is linearly

elastic as a first approximation for small deformations (approximately 1.0% frame-to-frame average strain),

$$J(\hat{E}) = \arg \min \left\{ \frac{1}{2} \|T(\hat{E}) - \hat{U}\|^2 + \beta V(\hat{E}) \right\}, \quad (2)$$

$$V(\hat{E}) = \int_{\Omega} (\sqrt{|\nabla \hat{E}|^2 + \gamma^2}) d\Omega, \quad (3)$$

subject to

$$E_{\min} \leq \hat{E} \leq E_{\max}, \quad (4)$$

where  $T(\hat{E})$  is the predicted axial displacement by a forward finite element simulation based on the current estimated modulus distribution  $\hat{E}$  and  $\hat{U}$  is the estimated axial displacement using the ultrasound-based speckle tracking algorithm described above. In equation (3),  $\nabla$  is a gradient operator,  $|(x, y)| = \sqrt{x^2 + y^2}$  is the Euclidean norm and  $\gamma$  is a small positive constant.

To stabilize the solution of equation (2), regularization (Vogel 2002) is often used, and the resulting solution is a tradeoff between fidelity to the measured displacement data (the first item on the right-hand side of equation (2)) and bias due to the regularity of the solution constrained through the regularization function (the second item on the right-hand side of equation (2)). In other words, regularization injects *a priori* knowledge to balance this tradeoff for a given situation. In this sense,  $\beta$  is a positive parameter controlling the tradeoff between the fidelity and variability in  $\hat{E}$ . In our experience, ablated tissues typically have a sharp transition in tissue stiffness between the normal and the ablated regions, whereas the tissue stiffness within both the normal and ablated regions gradually varies. Therefore, an edge-preserving regularization function  $V(\hat{E})$  is selected to enforce such a *a priori* knowledge in the hope of accurately capturing boundaries of a thermal zone in the reconstructed modulus map. In this study,  $\beta$  (equation (2)) and  $\gamma$  (equation (3)) were set to  $5 \times 10^{-7}$  and 0.1, respectively, for all data investigated. Detailed formulations to solve equations (2)–(4) can be found in our previous work (Jiang *et al* 2009).

### 2.3. Implementation of the EMI algorithm

To obtain a relative elastic modulus image, the basic procedures involved are summarized as follows.

- (1) Estimate displacement  $\hat{U}$  from a region of interest (ROI; see the white box in figure 3(a)) defined by a user.
- (2) Identify the location of the ablation electrode in both axial displacement and B-mode images. In the axial displacement image, pulling/pushing of the ablation electrode results in a rigid-body motion, that is, relatively constant displacements within a small region (see the arrow in figure 3(c)). In the B-mode image, a metal electrode typically results in reflection (see the arrow in figure 3(a)) shadowing below it. The locations of the ablation electrode on displacement and B-mode images should be spatially consistent.
- (3) Assume an initial uniform Young's modulus distribution  $\hat{E}$ . The displacements within the identified electrode region and the displacements at the edges of the ROI will be enforced as boundary conditions to solve the 2D FEA forward solution (i.e.  $T(\hat{E})$  in equation (2)).
- (4) Compare these predicted displacements  $T(\hat{E})$  with the ultrasonically measured displacements  $\hat{U}$ . Simultaneously, the assumed modulus distribution  $\hat{E}$  is updated. Iterations between (3) and (4) continue until one criterion or all convergence criteria are

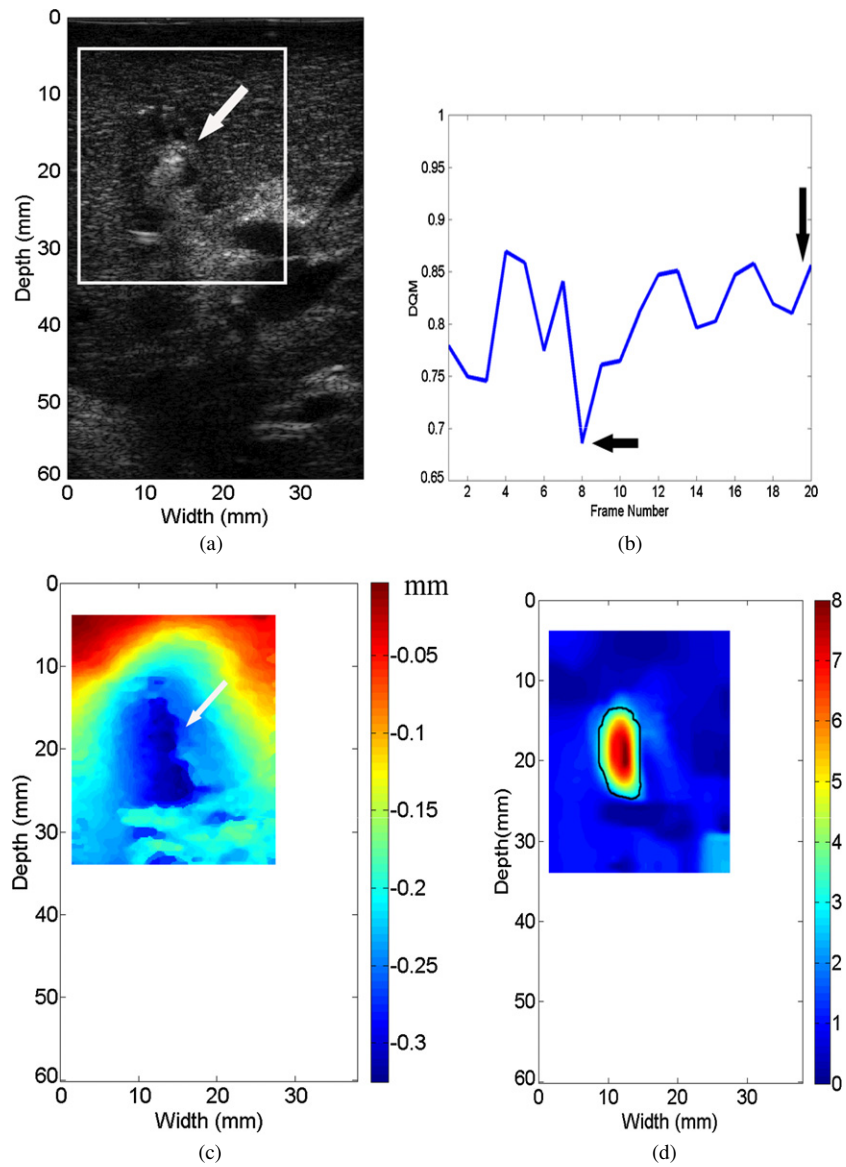


**Figure 3.** An example demonstrating that different displacement fields affect the quality of resultant elastic modulus images. All three displacement fields ((c), (e) and (g)) were obtained from the same thermal ablation zone shown by the B-mode image in (a). Three resultant elastic modulus images from (c), (e) and (g) are shown in (d), (f) and (h), respectively. Estimated DQM values from a sequence of strain images shown in movie 1 [stacks.iop.org/PMB/55/2281/mmedia](https://stacks.iop.org/PMB/55/2281/mmedia) can be found in (b). The vertical and horizontal arrows point to the DQM values corresponding to those in displacement fields displayed in (c) and (e), respectively. The arrows in (a) and (c) point to the location of the ablation applicator, while arrows in (e) and (g) point to decorrelation noise in the displacement fields.



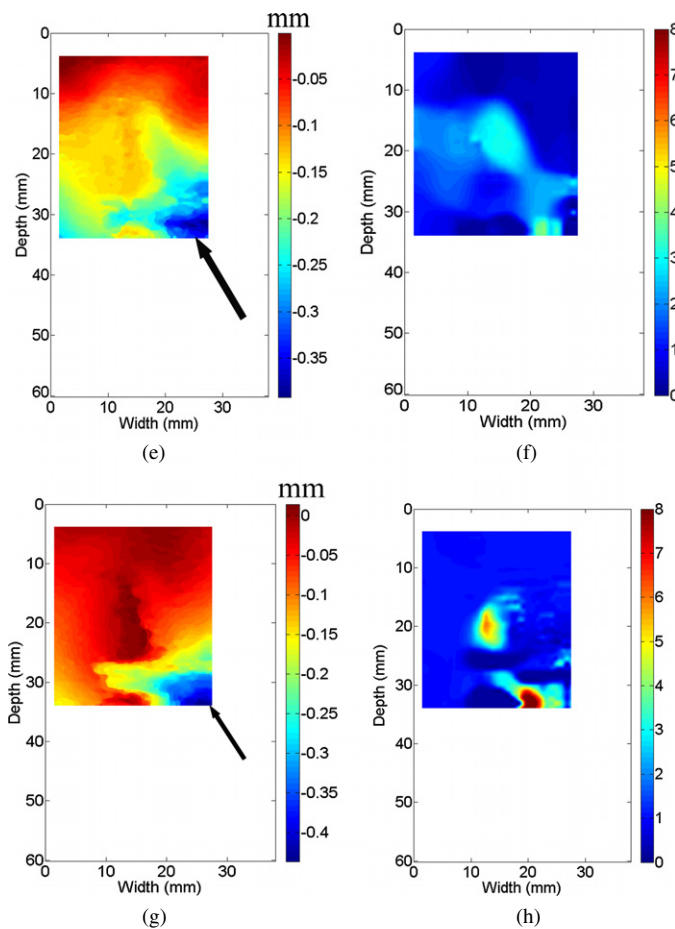


Figure 3. (Continued.)

satisfied. Usually, the criteria for convergence can be set with pre-determined thresholds  $\varepsilon_1$  and  $\varepsilon_2$  such that,  $\text{delta}(\hat{E}) < \varepsilon_1$  and/or  $J(\hat{E}) < \varepsilon_2$ .  $\text{delta}(\hat{E})$  above denotes the difference in the modulus distributions between two consecutive iterations. Convergence was typically reached within 30 iterations when we set both  $\varepsilon_1$  and  $\varepsilon_2$  to  $10^{-6}$  in this study.

- (5) Once convergence is reached, all modulus values within the ROI will be normalized by an averaged modulus value from a small area (typically 5 mm by 5 mm) identified by the user as the normal liver tissue. This step converts all of our results to relative elastic modulus images.

#### 2.4. Data selection and processing

RF echo data (approximately 160 frames for each thermal ablation zone) acquired for each ablation zone were processed offline using Matlab (Mathworks Inc., MA, USA) to obtain a sequence of strain images using the modified block matching algorithm described above (Jiang and Hall 2009). During strain image formation, a small two-dimensional kernel (0.90 mm lateral width by 0.40 mm axial length with 83% overlap laterally and 50% overlap axially) was used to track axial displacements (a pixel size of 0.15 mm (lateral)  $\times$  0.2 mm (axial)).

Then, axial strain images were obtained by fitting the local estimated axial displacement data to a line (i.e. linear regression) whose slope provides local strain at the center of this small (1.8 mm) segment of axial displacement estimates (Kallel and Ophir 1997).

A displacement quality metric (DQM; (Jiang *et al* 2006)) was calculated for each displacement and strain image. The DQM is the product of the normalized cross-correlation coefficient among the pre-deformation and motion-compensated post-deformation RF echo fields (a measure of motion tracking accuracy applied to the entire region of interest) and the normalized cross-correlation coefficient between two consecutive motion-compensated strain images (a measure of strain image consistency) (Jiang *et al* 2006). The DQM values lie between 0 and 1, with 1 providing the best result. The DQM method is used for semi-automated data selection as described below. Strain images are marked as ‘high’ quality only if at least three consecutive strain images possess DQM values greater than 0.75. One example of DQM estimates for 20 consecutive strain images estimated from a thermal ablation zone (see figure 3(a)) is shown in figure 3(b). The corresponding 20 frames of strain images displayed side by side with B-mode images can be found in movie 1 [stacks.iop.org/PMB/55/2281/mmedia](https://stacks.iop.org/PMB/55/2281/mmedia). If more than one ‘high’ quality strain image for a given thermal ablation zone exist, one displacement field (typically the displacement field whose corresponding strain image had the highest DQM value and least decorrelation noise as demonstrated in figure 3(c) below) is selected to reconstruct the corresponding elastic modulus image as described in sections 2.2 and 2.3.

Due to computational limitations, the displacement fields selected for the modulus reconstruction (see the ROIs in figures 3(a) and (c)) were spatially decimated to accommodate a smaller finite element mesh ( $41 \times 41$ ). For all cases, the size of finite elements (with a modulus constant within a finite element) used for EMI was variable but approximately  $0.75 \text{ mm} \times 0.75 \text{ mm}$ .

Three displacement images shown in figures 3(c), (e) and (g) all correspond to the same thermal ablation zone displayed in figure 3(a). Their DQM values are 0.85 (the 20th frame in figure 3(b) and movie 1), 0.68 (the eighth frame in figure 3(b) and movie 1) and 0.42 (not in movie 1), [stacks.iop.org/PMB/55/2281/mmedia](https://stacks.iop.org/PMB/55/2281/mmedia), respectively. In two displacement images (figures 3(e) and (g)) with relatively low DQM values, relatively high noise can be observed as indicated by arrows at the lower right corner. Consequently, when we reconstructed elastic modulus images using these three displacement fields, the quality of elastic modulus images was variable. In the case of the high quality displacement image (i.e. figure 3(c)), a single coherent region where relative modulus values were elevated can be clearly seen from figure 3(d). However, the resultant elastic modulus images from two relatively low quality displacement images could either contain considerable noise (figure 3(f)) or deviate from the expected shape of the thermal ablation zone (figure 3(h)).

The image quality of the resultant strain and elastic modulus images was assessed by the weighted contrast-to-noise ratio (CNR) defined below (Song *et al* 2004):

$$\text{CNR} = \frac{|S_t - S_b|}{(w_t \sigma_t^2 + w_b \sigma_b^2)^{1/2}}, \quad (5)$$

where  $S$  and  $\sigma^2$  denote means and variances of signals, and the subscripts  $b$  and  $t$  represent the background and target, respectively.  $w$  is a weighting of the area of the target and the background to the total area given by  $w_x = \text{area}_x / \text{area}_{\text{total}}$ . The inclusion of the weighted area is necessary because the target and the background contribute in different amounts to the noise estimates (Song *et al* 2004). It is worth noting that we converted all strain and elastic modulus images to the same resolution (a pixel size of 0.2 mm by 0.2 mm) prior to the estimation of CNR values and human segmentation of the ablation zones described below in section 2.5. To

calculate the CNR using equation (5) for each elasticity (strain and modulus) image, we used the manually segmented thermal ablation zone (see an example given by figure 3(d)) and the rest of the image as the target and the background, respectively.

### 2.5. Measurement of thermal ablation zones

Data from one RF ablation zone were excluded because the thermal ablation zone could not be seen using any modalities including B-mode, strain imaging and EMI. Only data obtained from the remaining 14 thermal ablation zones were processed and analyzed in this study. These 14 thermal ablation zones were manually delineated by three independent observers on strain and elastic modulus images, and corresponding pathology photographs using ImageJ (<http://rsbweb.nih.gov/ij/>). All three observers are ultrasound physicists/engineers who actively perform research related to ultrasound-based elasticity imaging. To understand the influence of color maps, both color and grayscale strain and elastic modulus images were presented to human readers.

In the first step, all observers were given grayscale strain and elastic modulus images, together with the co-registered B-mode ultrasound images, in a random order and were asked to delineate the thermal lesion boundaries in B-mode, strain and elastic modulus images. All observers had knowledge of the approximate position of each thermal ablation zone by simultaneously viewing the corresponding B-mode image. To look for sites of ablation zones in ultrasound B-mode images, observers were instructed to examine echogenicity changes. Observers were also instructed to look for a smooth contour representing a sharp transition (i.e. a large gradient in image contrast) between the normal liver tissue and the ablated tissue on the strain and elastic modulus image. When boundaries of a thermal ablation zone were not clearly defined on corresponding ultrasound B-mode, strain and elastic modulus images, observers were asked to complete their task by conservatively outlining a smooth contour around the position of the ablation applicator (known from the corresponding B-mode image).

In the second step, all observers were given a set of color (color map 'jet' in MATLAB) strain and elastic modulus images, together with the co-registered B-mode ultrasound images in a different random order. These color strain and elastic modulus images were exactly the same set of strain and elastic modulus images except the color map. Following the same guidelines mentioned above, observers were asked to delineate the thermal lesion boundaries in those color strain and elastic modulus images. A dynamic range for all strain images was set from either 0 to 2% or four times of the frame-average strain, whichever was less. Similarly, we also limited the dynamic range for all elastic modulus images either by using a relative scale ranging from 1 to 8 or four times of the frame-average relative modulus value, whichever was less.

In the third step, only 14 gross pathology images were given to these three observers, in a random order. Most *in vivo* thermal ablation zones contain a central white/gray zone representing coagulation necrosis and a surrounding red ring of about 1–3 mm thickness, representing hemorrhagic and inflammatory reactions (Goldberg *et al* 2003, Cha *et al* 2000). Because the outer red rim of the thermal ablation zone contains no viable cells (Goldberg *et al* 2003, Cha *et al* 2000), observers were instructed to include this thin layer from their segmented thermal ablation zones. In all three steps, after the thermal ablation zones were depicted, dimensions and areas of the thermal ablation zones were measured using the ImageJ software. Contouring with ImageJ described above was performed on the same monitor (MultiSync LCD 1860NX, NEC, Japan) with the same default monitor setting.

In the fourth step, we calculated the extent of overlap of areas of thermal ablation zones segmented manually by three observers in gross pathology, elastic modulus and strain images.

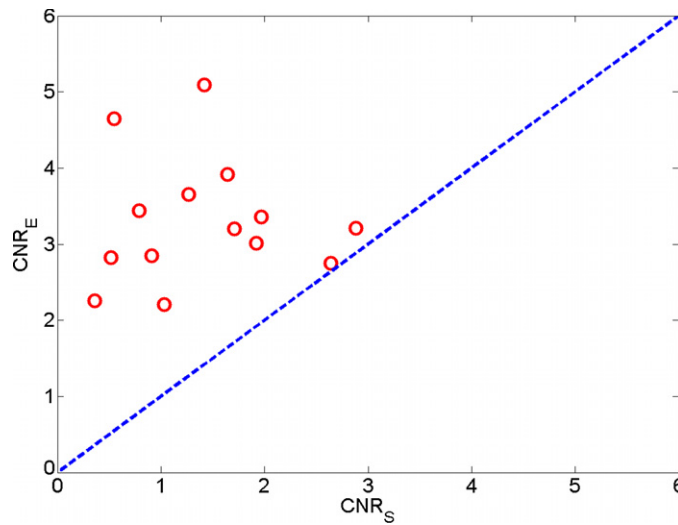


**Figure 4.** A plot of estimated contrast-to-noise ratios ( $CNR_S$ ) obtained from strain images ( $X$ -axis) with respect to estimated  $CNR_E$  obtained from elastic modulus images ( $Y$ -axis). The dashed line indicates a perfect slope representing equal contrast-to-noise ratio from both modalities.

The overlap was computed as follows:

$$\text{Overlap} = \frac{\text{Area}_1 \cap \text{Area}_2 \cap \text{Area}_3}{\text{Area}_1 \cup \text{Area}_2 \cup \text{Area}_3}, \tag{6}$$

where  $\cap$  and  $\cup$  represent intersection and union, respectively.

### 3. Results

Overall we found that there was virtually no difference (<5%) between measurements made on grayscale and color strain images, though measurements on grayscale strain images resulted in slightly lower errors as compared to measurements obtained from gross pathology photographs. On the other hand, measurements made on color elastic modulus images were slightly more accurate. Therefore, in this section, the comparison between strain imaging and EMI was based on measurements on grayscale strain and color elastic modulus images.

#### 3.1. Visibility of *in vivo* thermal ablation zones

As agreed upon by all three observers, the boundaries of all 14 thermal ablation zones were visualized by EMI (100%), while only 11 (78.5%) and 9 (64.5%) were detected by strain imaging and conventional B-mode ultrasound, respectively.

The estimated CNR values (equation (5)) from all strain and elastic modulus images are plotted in figure 4. Similar to the results subjectively rated by the human observers, the estimated CNRs also clearly indicate that modulus images (mean  $\pm$  standard deviation:  $3.32 \pm 0.81$ ; minimum: 1.96; maximum: 5.19) outperform the corresponding strain images (mean  $\pm$  standard deviation:  $1.40 \pm 0.78$ ; minimum: 0.36; maximum: 2.64).

We found, in two cases, that the estimated CNR values were comparable between the strain and modulus imaging. Figure 5 presents matching sonogram, strain, modulus and

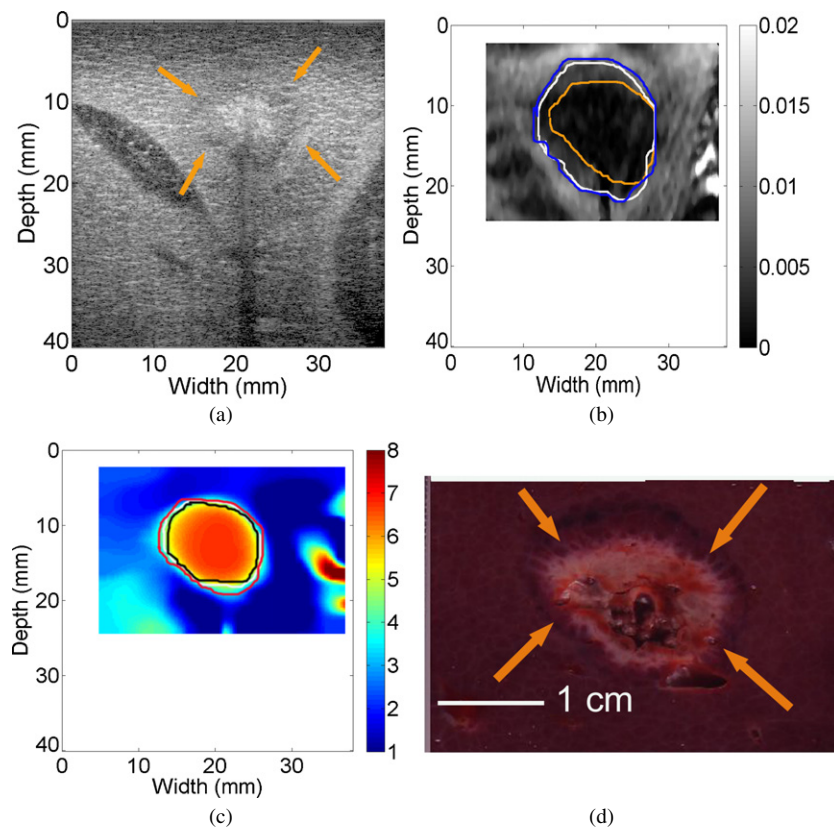


**Figure 5.** Images of an *in vivo* thermal ablation zone: (a) B-mode, (b) strain, (c) reconstructed relative elastic modulus and (d) photography of gross pathology. The contours on (b) and (c) were replicas of human observers' boundaries of ablation zones. Arrows in (a) and (d) point to the thermal ablation zone.

gross pathology images of a cross-section from one of these two thermal ablation zones. The thermal ablation zone can be visualized both from the strain (figure 5(b)) and elastic modulus (figure 5(c)) images. The size delineated by three different observers was consistent and comparable to that in the gross pathology photography. It seems that different observers merely chose different intensity thresholds when asked to manually segment the thermal ablation zone. The estimated CNR (equation (5)) for the strain and elastic modulus images shown in figure 5 were 2.64 and 2.75, respectively.

In three cases, the CNR values obtained from strain images were fairly low (0.55, 0.52 and 0.36, respectively). These three cases were three 'undetectable' cases agreed upon by all three human observers. One of these three cases is shown in figure 6. The calculated CNRs were 0.55 and 4.65 for the strain (figure 6(b)) and elastic modulus (figure 6(c)) images, respectively. It is easy to see that the thermal ablation zone can be visualized from the elastic modulus images (figure 6(c)) but cannot be confidently depicted based on the corresponding strain image (figure 6(b)). In fact, there was minimal overlap among the three contours depicted by the three different observers.

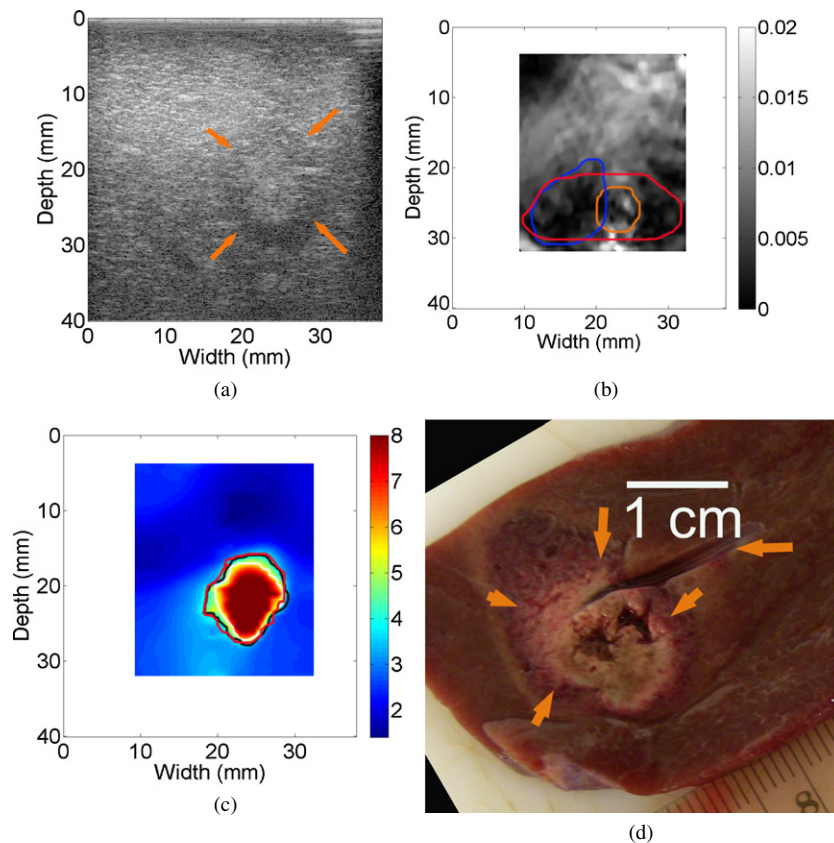


**Figure 6.** Images of an *in vivo* thermal ablation zone: (a) B-mode, (b) strain, (c) reconstructed relative elastic modulus and (d) photography of gross pathology. The contours on (b) and (c) were replicas of human observers' boundaries of ablation zones. Arrows in (a) and (d) point to the thermal ablation zone.

### 3.2. Measurement variability

In determining the measurement variability, the calculated differences in measured dimensions and areas among three different observers were listed in table 1. In table 1, the relative absolute difference between two observers A and B was calculated as follows: relative absolute difference = (measurement of A – measurement of B)/averaged measurement of gross pathology. Generally the measurement variability of the elastic modulus image data was comparable to measurements of the gross pathology data and was much smaller than those of strain imaging data. For example, the average percent difference (mean  $\pm$  standard deviation) over area measurements of the 14 thermal ablation zones for strain imaging, EMI and gross pathology were  $38.1 \pm 39.5\%$ ,  $15.8 \pm 13.2\%$  and  $11.8 \pm 10.5\%$ , respectively.

The averaged calculated overlap (equation (6)) among three independent observers for strain, elastic modulus and gross pathology images were  $0.52 \pm 0.21$  (mean  $\pm$  standard deviation),  $0.74 \pm 0.09$  and  $0.82 \pm 0.10$ , respectively. Again, in all 14 thermal ablation zones, the calculated overlaps by equation (6) from elastic modulus images were higher than the calculated overlaps from corresponding strain images.

**Table 1.** Inter-observer variations in measurements of thermal ablation zones. ‘Abs’ stands for the absolute difference (units: mm for dimensions and mm<sup>2</sup> for area measurements) and ‘Rel’ stands for the relative absolute difference with respect to measurements obtained from the gross pathology.

	Mean difference		Standard deviation		Maximum difference		Minimum difference	
	Abs (mm or mm <sup>2</sup> )	Rel (%)	Abs (mm or mm <sup>2</sup> )	Rel (%)	Abs (mm or mm <sup>2</sup> )	Rel (%)	Abs (mm or mm <sup>2</sup> )	Rel (%)
Short axis (strain)	3.3	27.7	2.5	22.3	10.4	98.7	0.0	0.0
Long axis (strain)	3.2	19.1	3.3	26.7	15.6	97.1	0.1	0.4
Area (strain)	61.3	38.6	54.4	39.5	212.2	176.5	1.5	0.7
Short axis (modulus)	1.2	10.0	1.1	8.2	5.6	40.4	0.0	0.4
Long axis (modulus)	2.1	12.2	2.0	12.7	6.9	54.0	0.2	1.0
Area (modulus)	28.8	15.8	22.4	13.2	79.8	43.8	0.6	0.2
Short axis (pathology)	1.5	12.9	1.2	12.0	4.8	50.9	0.0	0.0
Long axis (pathology)	1.2	7.1	0.8	6.2	3.5	29.2	0.0	0.0
Area (pathology)	20.9	11.8	15.0	10.5	51.7	48.5	0.4	0.3

For the thermal ablation zone illustrated in figure 5, the calculated overlap of the elastic modulus image was 0.69 and was slightly better than the calculated overlap (0.59) from the strain image. However, in an extreme case shown in figure 6 where the thermal ablation zone is barely visible (CNR = 0.55) in the strain image (figure 6(b)), the calculated overlap among the three observers for the strain image was only 0.03. It is easy to see that none of these three contours delineated by human observers on the strain image (figure 6(b)) were similar to that displayed by the gross pathology image. However, contours depicted by three human observers using the corresponding elastic modulus image (figure 6(c)) resulted in a calculated overlap value of 0.70 and were more consistent with the shape of the thermal ablation zone shown by the gross pathology photograph (figure 6(d)).

The thermal ablation zone shown in figure 7 is an interesting case. Although the calculated CNR value from the strain image (figure 7(b)) was only 0.36 and all three observers indicated low confidence on the detectability of the thermal ablation zone using the strain image (figure 7(b)). The contours delineated by human observers were remarkably consistent (0.60) as shown in figure 7(b), and these three delineated contours were moderately similar to shape and size of the thermal ablation zone on the gross pathology image (figure 7(d)). Of note, the calculated CNR and overlap values for the corresponding elastic modulus image (figure 7(c)) were 2.26 and 0.67, respectively.

### 3.3. Dimension and area correlation analysis

Measurements of the coagulation area using elasticity imaging and gross pathology were recorded by manually drawing contours (solid lines in three different colors) on respective images (see figures 5–7) as described before. Figure 8 shows scatter plots of averaged area measurements among three observers, comparing strain and EMI with freshly sliced gross pathology areas along respective imaging planes. In figure 8, the dash-dotted line indicates a perfect slope of 1, while the dashed and solid lines denote the linear fits for EMI and strain imaging data, respectively. Error bars are the standard deviation of three measurements made by three independent human observers, representing the uncertainty of the averaged

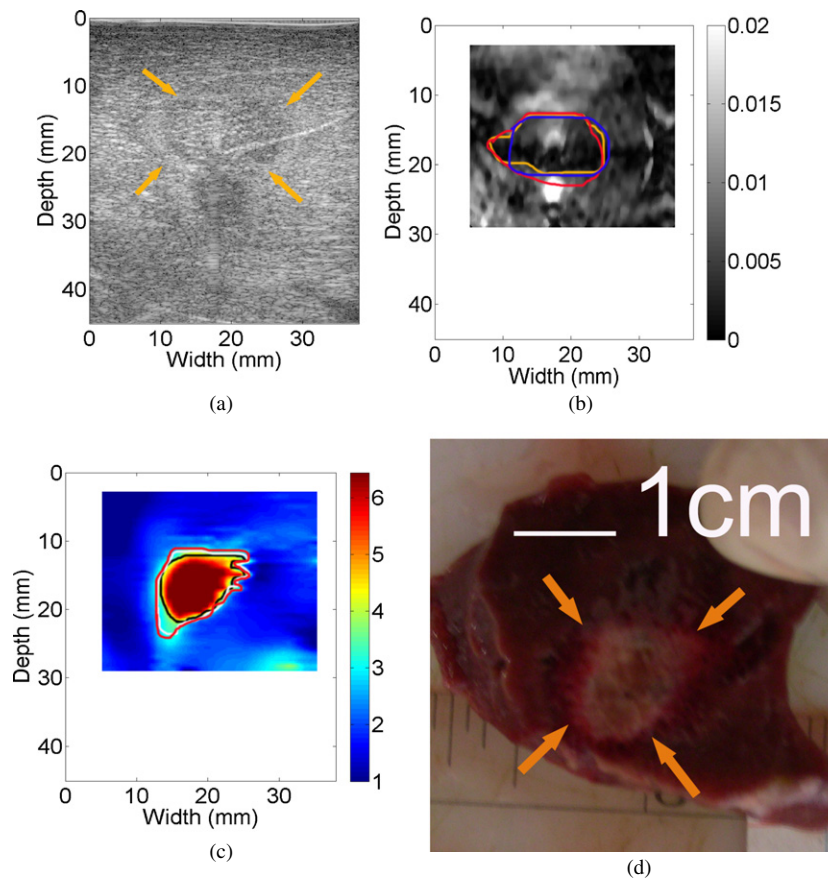


**Figure 7.** Images of an *in vivo* thermal ablation zone: (a) B-mode, (b) strain, (c) reconstructed relative elastic modulus and (d) photography of gross pathology. The contours on (b) and (c) were replicas of human observers' boundaries of ablation zones. Arrows in (a) and (d) point to the thermal ablation zone.

measurements. Consistent with data discussed before, the error bars of the EMI data are smaller than those of the strain imaging data. The correlation coefficient between EMI and gross pathology areas ( $r = 0.950$ ;  $p < 0.001$ ) is better than between strain imaging and gross pathology areas ( $r = 0.853$ ;  $p < 0.001$ ). Furthermore, the average of absolute percent errors, defined as the average of absolute differences in area measurements between elasticity imaging and gross pathology over the corresponding averaged area measurements obtained from the gross pathology, were 14.7% and 22.3% for EMI and strain imaging, respectively.

Scatter plots of the averaged dimensions (short and long axes) of ablation zones among three observers are presented in figures 9(a) and (b), respectively. As these scatter plots show, we found that the short axes of ablation zones obtained using elasticity imaging (elastic modulus and strain imaging) corresponded well to the short axes of the ablation zones on the digitized photographs of gross pathology specimens ( $r = 0.903$  ( $p < 0.001$ ) and  $0.733$  ( $p = 0.003$ ) and for elastic modulus and strain imaging, respectively). The long axes of the ablation zones on elastic modulus and strain images had a slightly worse correspondence to measurements obtained from the pathologic specimens ( $r = 0.887$  ( $p < 0.001$ ) and  $0.747$



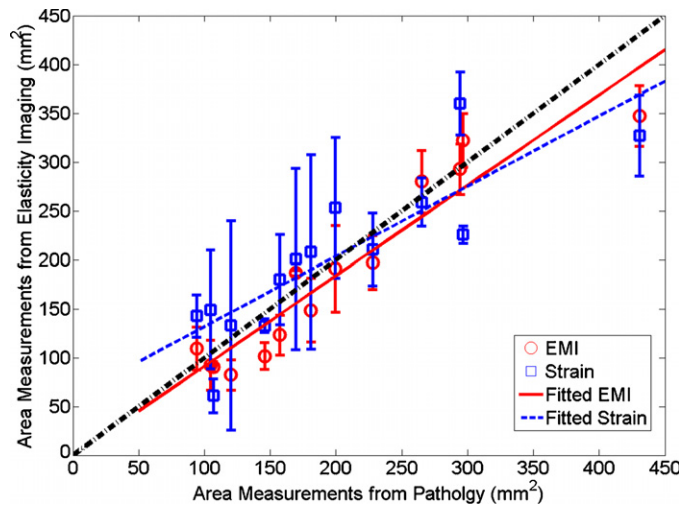


**Figure 8.** A plot comparing the area of thermal ablation zones between gross pathology and elasticity imaging (squares and circles represent averaged area measurements from three observers obtained from strain imaging and EMI). The estimated linear correlation coefficient between pathology and EMI was 0.950 ( $p < 0.0001$ ), while the estimated linear correlation coefficient between pathology and strain images was 0.857 ( $p < 0.0001$ ). Error bars denote one standard deviation among three observers made the measurements.

( $p = 0.002$ ) for elastic modulus and strain imaging, respectively). To obtain averaged lengths of the short and long axes for each thermal ablation zone from three independent observers, we simply averaged their measurements. Therefore, errors that may be caused by the angular shifts of the principal axes among different observers were not taken into account. In both plots, the dash-dotted line indicates a perfect slope of 1, while the dashed and solid lines denote the linear fits for EMI and strain imaging data, respectively.

### 3.4. Other notable cases

**3.4.1. Bifurcated thermal ablation zone.** The B-mode (figure 10(a)) and strain image (figure 10(b)) largely showed a single coherent ablation zone, while, in the reconstructed elastic modulus image (figure 10(c)), the bifurcation of the ablation zone is apparent and matches with the gross pathology image (figure 10(d)) more accurately in terms of the overall shape. We speculate that, during the insertion of the ablation applicator, a vessel was damaged, causing intra-parenchymal hemorrhage. Possibly, the formation of a blood bubble or the blood itself around the RF electrode (known as the heat sink effect) may have prevented local heat conduction, causing the bifurcated ablation zone. It is interesting to note that only one observer delineated the bifurcated shape of the thermal ablation zone on the elastic modulus image (figure 10(c)) and the other two observers were more conservative because of the unusual shape of the thermal ablation. However, two human observers overestimated the size of the thermal ablation zone on the corresponding strain image as shown by contours in figure 10(c). In clinical practice, the overestimation of the size of thermal ablation could cause premature termination of the thermal ablation procedure, thereby leaving viable cancerous tissue untreated.

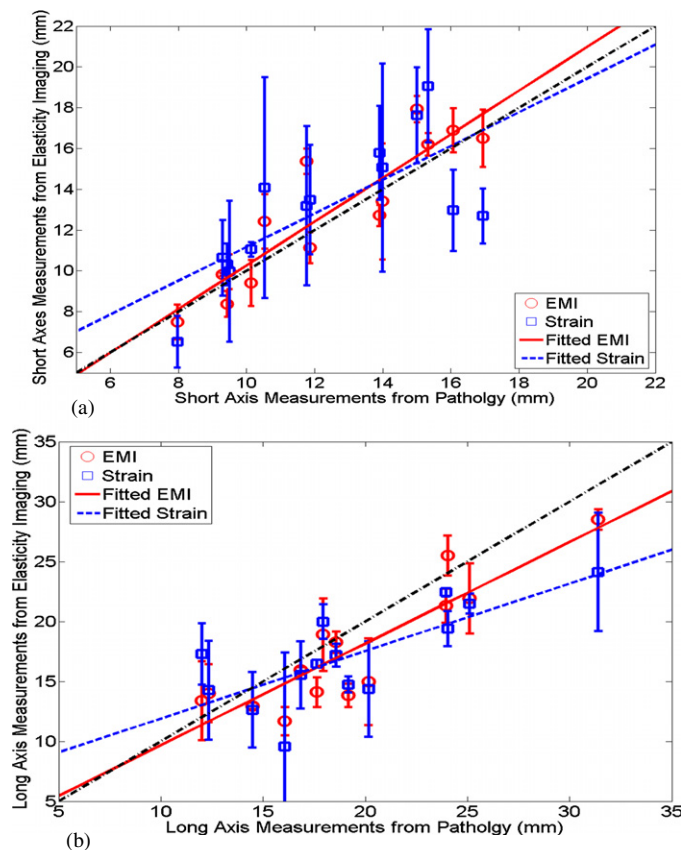


**Figure 9.** Plots of (a) the short axis and (b) the long axis of thermal ablation zones between gross pathology and elasticity imaging (squares and circles represent averaged dimension measurements from three observers obtained from strain imaging and EMI). The estimated linear correlation coefficients between pathology and EMI for short and long axes were 0.903 ( $p < 0.001$ ) and 0.887 ( $p < 0.001$ ), respectively, while the estimated linear correlation coefficients for long and short axes between pathology and strain images were 0.733 ( $p = 0.003$ ) and 0.747 ( $p = 0.002$ ), respectively.

**3.4.2. Detection of a small liver vessel only with strain imaging.** In figure 11(b), the strain imaging successfully detected the presence of a small vessel (approximately 1.2 mm diameter measured from the B-mode image; see the horizontal arrows in figures 11(a), (b) and (d)) because the collapse of the small vessel under the deformation resulted in a bright spot in the corresponding strain image. However, the same vessel was not visualized on the corresponding elastic modulus image (figure 11(c)). To completely coagulate a liver tumor, it is desirable to fully destruct some small blood vessels in and around the targeted tumor. Therefore, during an ablation procedure, strain imaging (as well as the B-mode in this case) may have sufficient sensitivity to detect these small vessels that have similar sizes to the liver vessel presented in figures 11(a)–(d). The loss of resolution in EMI, probably due to both regularization and large element size (approximately 0.75 mm), is also apparent in other relative elastic modulus images such as figure 5(c).

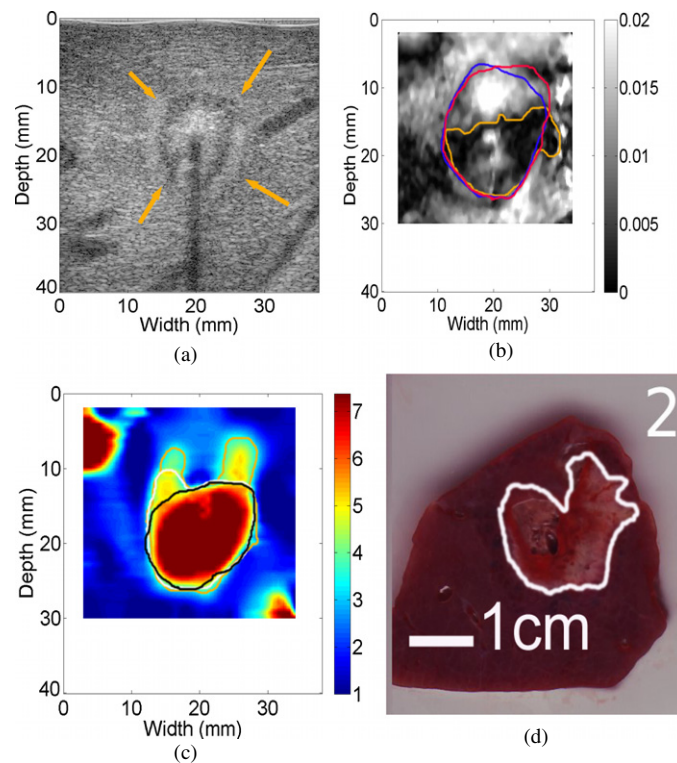


**Figure 10.** Images of an *in vivo* thermal ablation zone: (a) B-mode, (b) strain, (c) reconstructed relative elastic modulus and (d) photography of gross pathology. The contours on (b)–(d) were replicas of human observers' boundaries of ablation zones. Arrows in (a) point to the thermal ablation zone.

#### 4. Discussion

One contribution of our work is that we applied an EMI technique (Jiang *et al* 2009) to visualize *in vivo* thermal ablation zones. Since our ultimate goal is to use this modality to determine whether complete coagulation of a targeted tumor has been achieved in a clinical environment, it is significant to determine the fidelity of such a decision. Although a similar technique has been applied to characterize pathologically confirmed *in vivo* breast lesions (Oberai *et al* 2009), their imaging results have not been compared to actual pathological findings of these lesions. Our initial results showed good agreement of the area of thermal ablation zones (correlation = 0.950,  $p$ -value < 0.001) between EMI measurements and gross pathology. Compared to strain imaging (correlation = 0.853,  $p$ -value < 0.001), EMI results also showed improved detectability of thermal ablation zones and reduced inter-observer variability both in terms of calculated CNR values (see figure 4) and calculated measurement variability (see tables 1 and 2). More importantly, in one case, the elastic modulus image (figure 10(c)) clearly indicated a bifurcated thermal ablation zone and thereby avoided a potential gross pattern error in detection of the thermal ablation zone, compared to the corresponding strain image (figure 10(b)). These enhancements will likely improve clinicians' ability to evaluate the ablation zone immediately after the ablation procedure. We also found that there were subtle differences between corresponding EMI and pathological boundaries of ablation zones,

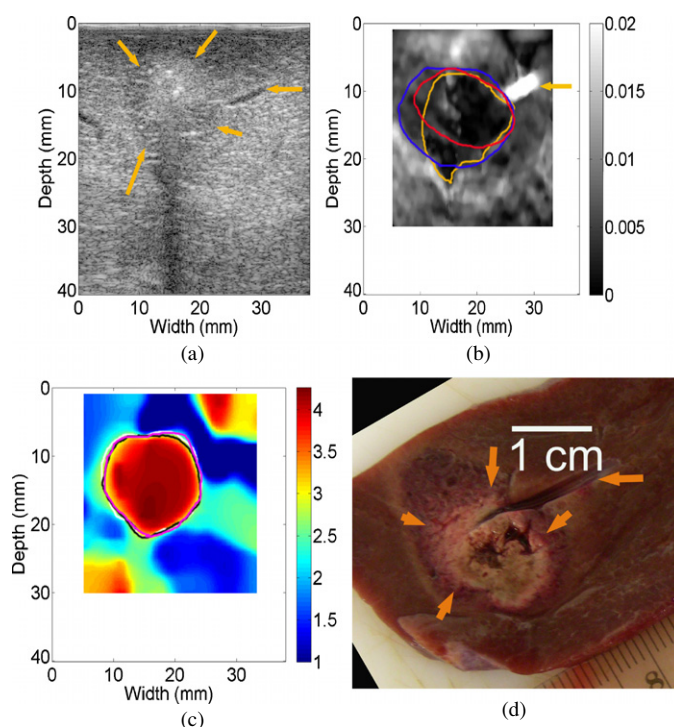


**Figure 11.** Images of an *in vivo* thermal ablation zone: (a) B-mode, (b) strain, (c) reconstructed relative elastic modulus and (d) photography of gross pathology. The contours on (b) and (c) were replicas of human observers’ boundaries of ablation zones. Horizontal arrows in (a), (b) and (d) point to a small liver vessel, while other arrows in (a) and (b) point to the thermal ablation zone.

**Table 2.** Area overlaps among three observers.

	Averaged overlap (mean ± standard deviation)	Minimum overlap	Maximum overlap
Gross pathology	0.82 ± 0.10	0.50	0.90
Strain	0.52 ± 0.21	0.03	0.78
Modulus	0.74 ± 0.09	0.59	0.91

because of limited resolution (approximately 0.75 mm element size) and sensitivity (noise in measured displacements) in EMI. The small detected differences (e.g. 1.2–2.5 mm on average in terms of dimension measurements; see table 3) between corresponding pathology and EMI boundaries are less of a concern for a newly developed technique, given that liver ablation tends to ablate an additional 5–10 mm of normal hepatic parenchyma to achieve a safe margin (Nakazawa *et al* 2007, Kei *et al* 2008).

Our three observers missed nearly 40% of thermal ablation zones using conventional B-mode images while the radiologist (AA) was able to identify all thermal ablation zones during data acquisition (aided by the improved visualization of gas bubbles and improved B-mode images). This reduced detectability could be explained as follows. First, the radiologist has considerable experience and training for ultrasound-guided thermal ablation, while our

**Table 3.** Summary of the measurement difference between EMI and gross pathology photos for 14 thermal ablation zones. ‘Abs’ stands for the absolute difference (units: mm for dimensions and mm<sup>2</sup> for area measurements) and ‘Rel’ stands for the relative absolute different with respect to measurements obtained from gross pathology.

	Mean difference		Standard deviation		Maximum difference		Minimum difference	
	Abs (mm or mm <sup>2</sup> )	Rel (%)	Abs (mm or mm <sup>2</sup> )	Rel (%)	Abs (mm or mm <sup>2</sup> )	Rel (%)	Abs (mm or mm <sup>2</sup> )	Rel (%)
Short axis (strain)	2.0	16.0	1.2	7.8	4.2	33.7	0.5	5.1
Long axis (strain)	3.5	18.6	2.1	12.2	7.3	44.1	1.1	6.2
Area (strain)	40.3	22.3	27.2	14.7	103.5	52.1	6.1	2.3
Short axis (modulus)	1.2	9.6	1.0	7.9	3.6	30.8	0.4	2.5
Long axis (modulus)	2.5	13.4	1.6	8.6	5.3	27.8	0.3	1.5
Area (modulus)	26.7	14.8	20.3	9.1	83.2	31.4	1.4	0.5

human observers are researchers with several years of training in ultrasound-based elasticity imaging. Second, the radiologist used high quality B-mode images produced by the imaging system whereas offline B-mode images used by the three observers were reconstructed using envelope detection of ultrasound echo data and are of poorer quality than the manufacturer’s B-mode images. Furthermore, the echogenicity of the RF thermal ablation zone was variable and could be hypoechoic, hyperechoic, isoechoic and/or mixed-echoic (Cha *et al* 2000, Liu *et al* 2004). Consequently, it is possible that small echogenicity differences between normal liver and ablated tissues were missed.

It is known that high CNRs in elasticity images (Bilgen 1999) indicate enhanced detectability of targets. We plot the estimated overlaps (equation (6)) among three observers with respect to estimated CNR values (equation (5)) in figure 12. The high inter-observer variability (overlap < 0.5) in four thermal ablation zones (lower right quarter in figure 12) could be attributed to low CNR values (<1.0) in the strain images. The exception is the thermal ablation zone presented in figure 7 where the CNR and overlap are 0.36 and 0.60, respectively, for the strain image shown in figure 7(b). Since only a small number of samples were investigated, further studies are needed.

We also recognize that the calculated CNR values will be inevitably affected by the selected dynamic range for strain and elastic modulus images. In this work, the dynamic range was limited to an empirical range (approximately 1–8) for relative elastic modulus images so that human observers could easily visualize the sharp transition (typically between 3 and 5 time stiffer than normal liver tissue (Kiss *et al* 2004)) of modulus values between the thermal ablation zone and its normal surrounding liver tissues. For all strain images, since the contrast transfer function between intrinsic elastic moduli and mechanical strain values is highly nonlinear (Ponnekanti *et al* 1995, Bharat and Varghese 2006), it is more difficult to determine an ideal dynamic range. We used both 2% of absolute strain (or four times of the frame-average strain) and three times of the frame-average strain (data were not shown) as the cutoffs. The differences in terms of area measurements between these two dynamic ranges were insignificant. The dynamic range of 0–2% slightly improved the averaged absolute percent error from 27.3% to 22.3%. Therefore, the dynamic range of 0–2% was reported throughout this paper.

One study by our colleagues (Pareek *et al* 2006) investigated the utility of strain imaging for visualizing thermal ablation zones for renal ablation in a porcine model. They reported

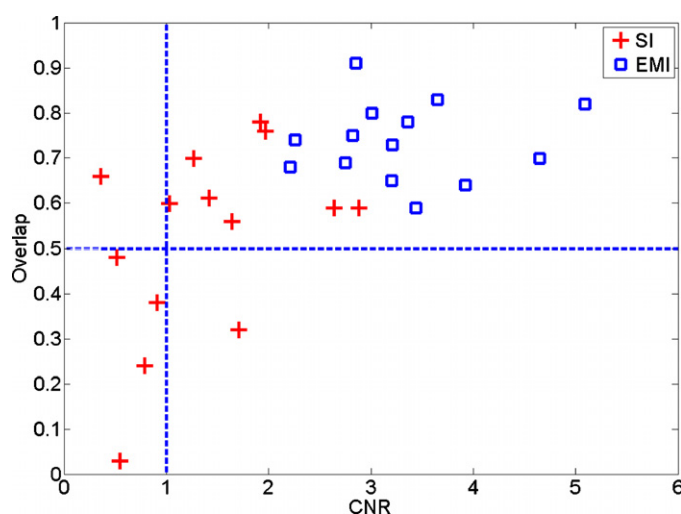


**Figure 12.** A plot illustrating the distribution of area overlap values (equation (6)) measured among three human observers with respect to the estimated CNR values (equation (5)) from strain (cross) and relative elastic modulus (square) images.

statistically significant correlations ( $r = 0.93$ ) between ablation area measurements of strain imaging and pathology. In another recent study by researchers from the University of Rochester (Zhang *et al* 2008), the sonoelastography technique was used to depict *in vivo* thermal ablation zones created both by high intensity focused ultrasound (HIFU) and radiofrequency ablation. In 18 thermal ablation zones created by radiofrequency ablation, they calculated a correlation of 0.88 between the sono-elastographical area measurements and pathological area measurements. Our correlation values (both strain imaging and EMI) were comparable with these two studies.

Our results showed that strain imaging slightly overestimated (on average 6.7%) sizes of the thermal ablation zones. From our theoretical study of numerical phantoms (Jiang *et al* 2007), we found that, because of the complex stress/displacement pattern induced by the ablation applicator, elastic contrast was fairly low in axial strain images at points corresponding to the lateral margins of thermal ablation zones. This phenomenon may interfere with human observers' ability to depict boundaries of the thermal ablation zones using axial strain images.

Consistent with the above-mentioned elasticity imaging studies (Pareek *et al* 2006, Zhang *et al* 2008), EMI slightly underestimated (on average 8.9%) sizes of thermal ablation zones. Furthermore, relative elastic contrast estimated by EMI between the untreated and ablated tissue ( $1 \text{ cm}^2$  regions at the center of each ablation zone) was only  $8.37 \pm 1.41$ . This value was lower than our internal mechanical compression testing results (approximately 15) of these same thermal ablation zones where  $1 \text{ cm}^3$  cubes of each ablation volume were tested following a previously published protocol (Kiss *et al* 2004). Similar elastic contrast values between treated and untreated porcine liver tissues were also reported by Zhang *et al* (2008). This underestimation was much larger than what previously reported for similar techniques (15–25% underestimation) in tissue mimicking phantoms (Oberai *et al* 2004, Doyley *et al* 2000). However, to spare the central cores of ablation zones for mechanical testing, all ultrasound (therefore EMI) imaging planes were at least 1 cm away from central planes of thermal ablation zones. It is logical to expect ablated tissue away from the needle applicator to be less stiff than the ablated tissue near the needle applicator, because the tissue stiffness

change is largely temperature dependent (Bharat *et al* 2005). Our ongoing research is to address both underestimations (i.e. size and elastic contrast) by using a more intelligent regularization method during inverse modulus reconstruction and improving the accuracy of speckle tracking.

We used a DQM metric (Jiang *et al* 2006) as the basis to pre-select displacement images. First, as demonstrated in figures 3(a)–(h), the quality of displacements affected the outcomes of EMI because the displacement estimates provide fundamental information for modulus reconstruction. Although good regularization methods (Doyley *et al* 2006) make the reconstruction process more robust, good quality displacement measurements should enable us to reduce the dependence on regularization. Second, we generally obtain a sequence of displacement fields for EMI in a clinical setting. The use of DQM could be a method for automated displacement data selection, thereby potentially eliminating user dependence.

We also found that, when grayscale elastic modulus images were used, human observers tended to further underestimate sizes of thermal ablation zones. The underestimation increased to 12.0% (up from 8.9% as described above). Compared to measurements made from color elastic modulus images using the same dynamic range described in section 2.5, the correlation of area measurements between grayscale elastic modulus images and gross pathology reduced to 0.90 (down from 0.95 as described above). Further studies of this topic may help us understand how to use appropriate color maps to improve the visualization of thermal ablation zones (Rogowitz and Treinish 2005).

One limitation of our study is that ultrasound images were not automatically registered with photographs of gross pathology. Since markers corresponding to respective imaging planes were created on the surfaces of liver lobes during data acquisition, we are reasonably confident that imaging planes of gross pathology should be in the vicinity of elasticity imaging planes. However, during post-processing of gross pathology and ultrasound-related imaging results, we were not able to find enough landmarks to estimate the errors of such manual alignments. This limitation could be resolved in our future studies. In the literature, multiple fiducial needles were used to register 3D images in and near ablation zones with sufficient accuracy (approximately 1 mm error) (Lazebnik *et al* 2003). Another limitation with the porcine model is that all thermal ablation zones were created in healthy parenchyma. The basic assumption of using EMI to differentiate ablation zones is that protein denaturation due to heating causes an increase of stiffness in ablated tissue (Kiss *et al* 2004). Because of this, the presence of certain liver masses which may also be harder (e.g. cholangiocarcinomas (Yeh *et al* 2002)) or softer (e.g. HCCs (Yeh *et al* 2002)) than normal liver tissue will likely make this differentiation more difficult.

The modulus reconstruction method (equations (2)–(4)) described in this paper assumes that both normal and ablated liver tissues are linearly elastic. Since nearly all soft tissue are nonlinear (Fung 1993), using a hyper-elastic material model similar to the model used by Oberai *et al* (2009) may improve our results at the expense of larger computational demands. However, inverse reconstruction of nonlinear material properties as in their work (Oberai *et al* 2009) might not be feasible because the large accumulative deformation (e.g. 15–20% of compression) required would be difficult to achieve in the liver with electrode displacement elastography.

Another limitation of our method is that we require a user to identify the location of the ablation applicator so that the deformation induced by the applicator (i.e. the source of mechanical stimulus) is a part of the boundary conditions.

In this study, open abdominal ablation procedures were performed. Clinically, approaches for hepatic ablation include both percutaneous and surgical ablation (laparoscopy and open) techniques. Although the percutaneous approach is preferred by many institutions because

of its minimally invasive nature (e.g. less morbidity, complications and associated healthcare costs), thermal ablation using surgical procedures including open-abdominal approach also provides distinct advantages (Siperstein *et al* 1997, Burdio *et al* 2008). In a large number of cases, hepatic ablation is still performed as open-abdominal procedures. With surgical ablation techniques, the entire liver can be imaged with a high-frequency intra-operative ultrasound transducer placed directly on the surface of the liver, resulting in better placement for ablation applicators and subsequent lower recurrence rates (Burdio *et al* 2008). Although we do not make any assumptions about the liver geometry, we use all displacement estimates along edges of a user-defined ROI (see figure 3(a)) as a part of the boundary conditions. If our method would be applied to percutaneous ablation, the presence of the body wall may induce phase aberration, signal loss and distortion in ultrasound data, thereby resulting in less accurate displacement estimation under certain conditions (Varghese *et al* 2001). If these inaccurate displacements happen to be around the edge of the ROI, they would likely degrade our ability to visualize the thermal ablation zone as the examples demonstrated in figures 3(f) and (g). This use of EMI during open abdominal ablation, a less complicated imaging condition, is a necessary first step to test its clinical utility. Our ongoing research is to test the above-mentioned EMI method in the presence of a tumor background and using percutaneous ablation.

Currently, the elastic modulus reconstruction algorithm is implemented using MATLAB (Mathworks Inc., MA, USA) and provides an elastic modulus image in 15–20 min. However, achieving a reasonably fast frame rate (20 s/frame) for EMI is indeed possible. The formation of a 2D elastic modulus image in 30 s using advanced programming language C in conjunction with a much less advanced personal computer (Pentium 1-GHz) was reported in by Oberai *et al* (2004).

## 5. Conclusions

The use of our EMI method to visualize *in vivo* thermal ablation zones was presented. In all 14 cases, when compared to strain imaging, the elastic modulus images show equal or better detectability in terms of visualization of the *in vivo* thermal ablation zones. Our results also demonstrate that the proposed EMI method has the potential to accurately (correlation = 0.950 and mean error = 8.9%) depict boundaries of complex thermal ablation zones. This initial result is encouraging and warrants further carefully planned studies involving a reasonably large number of pre-clinical animal experiments, in particular, using tumor-bearing animal models. If successful, the ultrasound-based EMI method can be a useful means for monitoring and evaluating thermal ablation procedures involving human patients.

## Acknowledgments

We gratefully acknowledge the support by NIH grants R01CA100373, R01CA112192 and R01CA112192-03S1. Ted Fisher and Ryan DeWall are supported, in part, by an NIH training grant T32CA09206. We are also grateful to colleagues at the University of Wisconsin (especially Drs Mark Kliewer and Shyam Bharat and Ms Lisa Sampson) for their assistance in equipment access and data acquisition during ablation experiments.

## References

- Barbone P E and Bamber J C 2002 Quantitative elasticity imaging: what can and cannot be inferred from strain images *Phys. Med. Biol.* **47** 2147–64



- Bharat S, Techavipoo U, Kiss M Z, Liu W and Varghese T 2005 Monitoring stiffness changes in lesions after radiofrequency ablation at different temperatures and durations of ablation *Ultrasound Med. Biol.* **31** 415–22
- Bharat S and Varghese T 2006 Contrast-transfer improvement for electrode displacement elastography *Phys. Med. Biol.* **51** 6403–18
- Bilgen M 1999 Target detectability in acoustic elastography *IEEE Trans. Ultrason. Ferroelectr. Freq. Control* **46** 1128–33
- Brace C L, Laeseke P F, Sampson L A, Frey T M, van der Weide D W and Lee F T Jr 2007 Microwave ablation with a single small-gauge triaxial antenna: *in vivo* porcine liver model *Radiology* **242** 435–40
- Brunke S S, Insana M F, Dahl J J, Hansen C, Ashfaq M and Ermert H 2007 An ultrasound research interface for a clinical system *IEEE Trans. Ultrason. Ferroelectr. Freq. Control* **54** 198–210
- Burdio F, Mulier S, Navarro A, Figueras J, Berjano E, Poves I and Grande L 2008 Influence of approach on outcome in radiofrequency ablation of liver tumors *Surg. Oncol.* **17** 295–9
- Bush N L, Rivens I, ter Haar G R and Bamber J C 1993 Acoustic properties of lesions generated with an ultrasound therapy system *Ultrasound Med. Biol.* **19** 789–801
- Callstrom M R *et al* 2006 Painful metastases involving bone: percutaneous image-guided cryoablation—prospective trial interim analysis *Radiology* **241** 572–80
- Carter D L, MacFall J R, Clegg S T, Wan X, Prescott D M, Charles H C and Samulski T V 1998 Magnetic resonance thermometry during hyperthermia for human high-grade sarcoma *Int. J. Radiat. Oncol. Biol. Phys.* **40** 815–22
- Cha C H, Lee F T Jr, Gurney J M, Markhardt B K, Warner T F, Kelcz F and Mahvi D M 2000 CT versus sonography for monitoring radiofrequency ablation in a porcine liver *AJR Am. J. Roentgenol.* **175** 705–11
- Doyley M M, Meaney P M and Bamber J C 2000 Evaluation of an iterative reconstruction method for quantitative elastography *Phys. Med. Biol.* **45** 1521–40
- Doyley M M, Srinivasan S, Dimidenko E, Soni N and Ophir J 2006 Enhancing the performance of model-based elastography by incorporating additional *a priori* information in the modulus image reconstruction process *Phys. Med. Biol.* **51** 95–112
- Dupuy D E and Goldberg S N 2001 Image-guided radiofrequency tumor ablation: challenges and opportunities—part II *J. Vasc. Interv. Radiol.* **12** 1135–48
- Fahey B J, Hsu S J, Wolf P D, Nelson R C and Trahey G E 2006 Liver ablation guidance with acoustic radiation force impulse imaging: challenges and opportunities *Phys. Med. Biol.* **51** 3785–808
- Fung Y C 1993 *Biomechanics: Mechanical Properties of Living Tissues* (New York: Springer)
- Gao L, Parker K J, Lerner R M and Levinson S F 1996 Imaging of the elastic properties of tissue—a review *Ultrasound Med. Biol.* **22** 959–77
- Gazelle G S, Goldberg S N, Solbiati L and Livraghi T 2000 Tumor ablation with radio-frequency energy *Radiology* **217** 633–46
- Gervais D A, McGovern F J, Arellano R S, McDougal W S and Mueller P R 2005 Radiofrequency ablation of renal cell carcinoma: part 1. Indications, results, and role in patient management over a 6-year period and ablation of 100 tumors *AJR Am. J. Roentgenol.* **185** 64–71
- Gervais D A, McGovern F J, Wood B J, Goldberg S N, McDougal W S and Mueller P R 2000 Radio-frequency ablation of renal cell carcinoma: early clinical experience *Radiology* **217** 665–72
- Goldberg S N *et al* 2003 Image-guided tumor ablation: proposal for standardization of terms and reporting criteria *Radiology* **228** 335–45
- Goldberg S N, Gazelle G S and Mueller P R 2000 Thermal ablation therapy for focal malignancy: a unified approach to underlying principles, techniques, and diagnostic imaging guidance *AJR Am. J. Roentgenol.* **174** 323–31
- Goldberg S N, Gazelle G S, Solbiati L, Livraghi T, Tanabe K K, Hahn P F and Mueller P R 1998 Ablation of liver tumors using percutaneous RF therapy *AJR Am. J. Roentgenol.* **170** 1023–8
- Greenleaf J F, Fatemi M and Insana M 2003 Selected methods for imaging elastic properties of biological tissues *Annu. Rev. Biomed. Eng.* **5** 57–78
- Hall T J 2003 AAPM/RSNA physics tutorial for residents: topics in US: beyond the basics: elasticity imaging with US *Radiographics* **23** 1657–71
- Hyodoh H, Hyodoh K, Takahashi K, Furuse M, Kawamoto C, Isoda N, Hozumi M, Ido K and Hirota N 1998 Microwave coagulation therapy on hepatomas: CT and MR appearance after therapy *J. Magn. Reson. Imaging* **8** 451–8
- Jeffrey S S, Birdwell R L, Ikeda D M, Daniel B L, Nowels K W, Dirbas F M and Griffey S M 1999 Radiofrequency ablation of breast cancer: first report of an emerging technology *Arch. Surg.* **134** 1064–8
- Jiang J and Hall T 2009 A generalized speckle tracking algorithm for ultrasonic strain imaging using dynamic programming *Ultrasound Med. Biol.* **35** 1863–79
- Jiang J, Hall T J and Sommer A M 2006 A novel performance descriptor for ultrasonic strain imaging: a preliminary study *IEEE Trans. Ultrason. Ferroelectr. Freq. Control* **53** 1088–102

- Jiang J, Varghese T, Brace C, Madsen E, Hall T, Bharat S, Hobson M, Zagzebski J and Lee F Jr 2009 Young's modulus reconstruction for radio-frequency ablation electrode-induced displacement fields: a feasibility study *IEEE Trans. Med. Imaging* **28** 1325–34
- Jiang J, Varghese T, Chen Q, Hall T J and Zagzebski J A 2007 Finite element analysis of tissue deformation with a radiofrequency ablation electrode for strain imaging *IEEE Trans. Ultrason. Ferroelectr. Freq. Control* **54** 281–9
- Kallel F and Bertrand M 1996 Tissue elasticity reconstruction using linear perturbation method *IEEE Trans. Med. Imaging* **15** 299–313
- Kallel F and Ophir J 1997 A least-squares strain estimator for elastography *Ultrason. Imaging* **19** 195–208
- Kallel F, Stafford R J, Price R E, Righetti R, Ophir J and Hazle J D 1999 The feasibility of elastographic visualization of HIFU-induced thermal lesions in soft tissues. Image-guided high-intensity focused ultrasound *Ultrasound Med. Biol.* **25** 641–7
- Kei S K, Rhim H, Choi D, Lee W J, Lim H K and Kim Y S 2008 Local tumor progression after radiofrequency ablation of liver tumors: analysis of morphologic pattern and site of recurrence *AJR Am. J. Roentgenol.* **190** 1544–51
- Kiss M Z, Varghese T and Hall T J 2004 Viscoelastic characterization of *in vitro* canine tissue *Phys. Med. Biol.* **49** 4207–18
- Laeseke P F, Sampson L A, Frey T M, Mukherjee R, Winter T C III, Lee F T Jr and Brace C L 2007 Multiple-electrode radiofrequency ablation: comparison with a conventional cluster electrode in an *in vivo* porcine kidney model *J. Vasc. Interv. Radiol.* **18** 1005–10
- Lazebnik R S, Lancaster T L, Breen M S, Lewin J S and Wilson D L 2003 Volume registration using needle paths and point landmarks for evaluation of interventional MRI treatments *IEEE Trans. Med. Imaging* **22** 653–60
- Lencioni R, Cioni D, Crocetti L, Franchini C, Pina C D, Lera J and Bartolozzi C 2005 Early-stage hepatocellular carcinoma in patients with cirrhosis: long-term results of percutaneous image-guided radiofrequency ablation *Radiology* **234** 961–7
- Liang P, Dong B, Yu X, Yu D, Wang Y, Feng L and Xiao Q 2005 Prognostic factors for survival in patients with hepatocellular carcinoma after percutaneous microwave ablation *Radiology* **235** 299–307
- Liu W, Techavipoo U, Varghese T, Zagzebski J A, Chen Q and Lee F T Jr 2004 Elastographic versus x-ray CT imaging of radio frequency ablation coagulations: an *in vitro* study *Med. Phys.* **31** 1322–32
- Lu M D, Xu H X, Xie X Y, Yin X Y, Chen J W, Kuang M, Xu Z F, Liu G J and Zheng Y L 2005 Percutaneous microwave and radiofrequency ablation for hepatocellular carcinoma: a retrospective comparative study *J. Gastroenterol.* **40** 1054–60
- Mikami T, Takahashi A, Hashi K, Gasa S and Houkin K 2004 Performance of bipolar forceps during coagulation and its dependence on the tip material: a quantitative experimental assay. Technical note *J. Neurosurg.* **100** 133–8
- Montgomery R S, Rahal A, Dodd G D III, Leyendecker J R and Hubbard L G 2004 Radiofrequency ablation of hepatic tumors: variability of lesion size using a single ablation device *AJR Am. J. Roentgenol.* **182** 657–61
- Nakazawa T, Kokubu S, Shibuya A, Ono K, Watanabe M, Hidaka H, Tsuchihashi T and Saigenji K 2007 Radiofrequency ablation of hepatocellular carcinoma: correlation between local tumor progression after ablation and ablative margin *Am. J. Roentgenol.* **188** 480–8
- Nguyen C L, Scott W J, Young N A, Rader T, Giles L R and Goldberg M 2005 Radiofrequency ablation of primary lung cancer: results from an ablate and resect pilot study *Chest* **128** 3507–11
- Oberai A A, Gokhale N H, Doyley M M and Bamber J C 2004 Evaluation of the adjoint equation based algorithm for elasticity imaging *Phys. Med. Biol.* **49** 2955–74
- Oberai A A, Gokhale N H, Goenezen S, Barbone P E, Hall T J, Sommer A M and Jiang J 2009 Linear and nonlinear elasticity imaging of soft tissue *in vivo*: demonstration of feasibility *Phys. Med. Biol.* **54** 1191–207
- Ophir J, Alam S K, Garra B, Kallel F, Konofagou E, Krouskop T and Varghese T 1999 Elastography: ultrasonic estimation and imaging of the elastic properties of tissues *Proc. Inst. Mech. Eng. H* **213** 203–33
- Ophir J, Cespedes I, Ponnekanti H, Yazdi Y and Li X 1991 Elastography: a quantitative method for imaging the elasticity of biological tissues *Ultrason. Imaging* **13** 111–34
- Pareek G, Wilkinson E R, Bharat S, Varghese T, Laeseke P F, Lee F T Jr, Warner T F, Zagzebski J A and Nakada S Y 2006 Elastographic measurements of *in-vivo* radiofrequency ablation lesions of the kidney *J. Endourol.* **20** 959–64
- Pilatou M C, Stewart E A, Maier S E, Fennessy F M, Hynynen K, Tempny C M and McDannold N 2009 MRI-based thermal dosimetry and diffusion-weighted imaging of MRI-guided focused ultrasound thermal ablation of uterine fibroids *J. Magn. Reson. Imaging* **29** 404–11
- Ponnekanti H, Ophir J, Huang Y and Cespedes I 1995 Fundamental mechanical limitations on the visualization of elasticity contrast in elastography *Ultrasound Med. Biol.* **21** 533–43
- Rogowitz B E and Treinish L A 2005 Why should engineers and scientists be worried about color? *Technical Report* (New York: IBM Thomas J Watson Research Center)

- Rosenthal D I, Hornicek F J, Wolfe M W, Jennings L C, Gebhardt M C and Mankin H J 1998 Percutaneous radiofrequency coagulation of osteoid osteoma compared with operative treatment *J. Bone Joint Surg. Am.* **80** 815–21
- Sato M, Watanabe Y, Ueda S, Iseki S, Abe Y, Sato N, Kimura S, Okubo K and Onji M 1996 Microwave coagulation therapy for hepatocellular carcinoma *Gastroenterology* **110** 1507–14
- Siperstein A E, Rogers S J, Hansen P D and Gitomirsky A 1997 Laparoscopic thermal ablation of hepatic neuroendocrine tumor metastases *Surgery* **122** 1147–54 discussion 54–5
- Solbiati L *et al* 1997 Percutaneous US-guided radio-frequency tissue ablation of liver metastases: treatment and follow-up in 16 patients *Radiology* **202** 195–203
- Solbiati L, Ierace T, Tonolini M and Cova L 2004 Guidance and monitoring of radiofrequency liver tumor ablation with contrast-enhanced ultrasound *Eur. J. Radiol.* **51** S19–23
- Song X, Pogue B W, Jiang S, Doyley M M, Dehghani H, Tosteson T D and Paulsen K D 2004 Automated region detection based on the contrast-to-noise ratio in near-infrared tomography *Appl. Opt.* **43** 1053–62
- Stern J M, Merritt M E, Zeltser I, Raman J D and Cadeddu J A 2008 Phase one pilot study using magnetic resonance spectroscopy to predict the histology of radiofrequency-ablated renal tissue *Eur. Urol.* **55** 433–40
- Varghese T, Bilgen M and Ophir J 2001 Phase aberration effects in elastography *Ultrasound Med. Biol.* **27** 819–27
- Varghese T, Zagzebski J A and Lee F T Jr 2002 Elastographic imaging of thermal lesions in the liver *in vivo* following radiofrequency ablation: preliminary results *Ultrasound Med. Biol.* **28** 1467–73
- Vogel C R 2002 *Computational Methods for Inverse Problems* (Philadelphia, PA: SIAM)
- Wacker F K, Nour S G, Eisenberg R, Duerk J L and Lewin J S 2004 MRI-guided radiofrequency thermal ablation of normal lung tissue: *in vivo* study in a rabbit model *AJR Am. J. Roentgenol.* **183** 599–603
- Weidensteiner C, Quesson B, Caire-Gana B, Kerioui N, Rullier A, Trillaud H and Moonen C T 2003 Real-time MR temperature mapping of rabbit liver *in vivo* during thermal ablation *Magn. Reson. Med.* **50** 322–30
- White D C and D'Amico T A 2008 Radiofrequency ablation for primary lung cancer and pulmonary metastases *Clin. Lung Cancer* **9** 16–23
- Wolf F J, Grand D J, Machan J T, Dipetrillo T A, Mayo-Smith W W and Dupuy D E 2008 Microwave ablation of lung malignancies: effectiveness, CT findings, and safety in 50 patients *Radiology* **247** 871–9
- Yeh W C, Li P C, Jeng Y M, Hsu H C, Kuo P L, Li M L, Yang P M and Lee P H 2002 Elastic modulus measurements of human liver and correlation with pathology *Ultrasound Med. Biol.* **28** 467–74
- Zagoria R J, Traver M A, Werle D M, Perini M, Hayasaka S and Clark P E 2007 Oncologic efficacy of CT-guided percutaneous radiofrequency ablation of renal cell carcinomas *AJR Am. J. Roentgenol.* **189** 429–36
- Zhang M, Castaneda B, Christensen J, Saad W, Bylund B, Hoyt K, Strang J G, Rubens D J and Parker K J 2008 Real-time sonoelastography of hepatic thermal lesions in a swine model *Med. Phys.* **35** 4132
- Zhu Y, Hall T J and Jiang J 2003 A finite-element approach for Young's modulus reconstruction *IEEE Trans. Med. Imaging* **22** 890–901